Simulation of interacting elastic sheets in shear flow

Insights into buckling, sliding, and reassembly of graphene nanosheets in sheared liquids

Salussolia, G.; Kamal, C.; Stafford, J.; Pugno, N.; Botto, L.

DOI
10.1063/5.0087192

Publication date
2022

Document Version
Final published version

Published in
Physics of Fluids

Physics of Fluids

Simulation of interacting elastic sheets in shear flow: Insights into buckling, sliding, and reassembly of graphene nanosheets in sheared liquids

Cite as: Phys. Fluids **34**, 053311 (2022); https://doi.org/10.1063/5.0087192
Submitted: 02 February 2022 • Accepted: 20 April 2022 • Published Online: 11 May 2022

G. Salussolia, C. Kamal, J. Stafford, et al.

Physics of Fluids ARTICLE scitation.org/journal/phf

Simulation of interacting elastic sheets in shear flow: Insights into buckling, sliding, and reassembly of graphene nanosheets in sheared liquids

Cite as: Phys. Fluids **34**, 053311 (2022); doi: 10.1063/5.0087192
Submitted: 2 February 2022 · Accepted: 20 April 2022 ·
Published Online: 11 May 2022

G. Salussolia,[1,2] C. Kamal,[3] J. Stafford,[4] N. Pugno,[5,a)] and L. Botto[6,a)]

AFFILIATIONS

[1]Facultad de Ingeniería y Tecnología, Universidad San Sebastián, Valdivia, Chile
[2]School of Engineering and Materials Science, Queen Mary University of London, London, United Kingdom
[3]Department of Applied Mathematics and Theoretical Physics, University of Cambridge, Cambridge, United Kingdom
[4]School of Mechanical Engineering, University of Birmingham, Birmingham, United Kingdom
[5]Laboratory for Bioinspired, Bionic, Nano, Meta Materials & Mechanics, Department of Civil, Environmental and Mechanical Engineering, University of Trento, Trento, Italy
[6]Process and Energy Department, Delft University of Technology, Delft, the Netherlands

[a)]**Authors to whom correspondence should be addressed**: nicola.pugno@unitn.it and l.botto@tudelft.nl

ABSTRACT

In liquid-based material processing, hydrodynamic forces are known to produce severe bending deformations of two-dimensional (2D) materials such as graphene. The non-linear rotational and deformation dynamics of these atomically thin sheets is extremely sensitive to hydrodynamic particle-particle interactions. To investigate this problem, we developed a computational model of the flow dynamics of elastic sheets suspended in a linear shear flow, solving the full fluid-solid coupling problem in the two-dimensional, slender-body, Stokes flow regime. Both single and pairs of sheets in close proximity are analyzed. Despite the model being two-dimensional, the critical non-dimensional shear rate yielding single-particle buckling is comparable in order of magnitude to that reported for fully three-dimensional, disk-like sheets. For pairs of interacting sheets, hydrodynamic interactions lead either to parallel sliding or bending, depending on the value of an elasto-viscous number based on particle length. For sufficiently low bending rigidity or large shear rates, large deformations of initially stacked sheets lead to sheet reattachment after separation, unlike for the rigid case. A peeling-like dynamics where lubrication provides a viscous bonding force is observed for sheet pairs when one of the two sheets is more rigid than the other. Practical implications for graphene processing and exfoliation are discussed.

I. INTRODUCTION

Applications of graphene and other two-dimensional (2D) materials suspended in shear liquids pose new scientific questions for the fluid dynamics and non-linear mechanics of thin structures.[1–4] Two-dimensional nanomaterials are sheet-like crystals of atomic thickness which often take the form of colloidal particles. In this form, they are most often processed in the liquid state (e.g., in inks,[5–7] coatings,[8,9] polymer nanocomposite processing[10,11] and in liquid-phase exfoliation[12,13]). During processing, sufficiently energetic motion of the fluid can deform these highly deformable nanostructures: 2D material particles can bend, fold, and buckle under sufficiently large viscous shear and pressure forces. In this article, we use numerical simulations to get insights into the relation between shear rate, bending rigidity, particle length, and inter-particle separation for sheet-like particles that are nearly touching, to extend recent work on single deformable sheets.[2,14–18] 2D nanosheets are prone to stacking in liquids, and therefore the study of elastic sheets at close proximity is relevant to the many situations in which the solid-liquid dispersion is not very dilute and hydrodynamic interactions are thus important.

Two-dimensional materials have sub-nanometric thickness, so atomistic methods seem an obvious choice for their simulation. However, in tackling flexibility, there is a problem of scales. Atomistic simulation techniques such as molecular dynamics allow only relatively short sheets to be simulated (typically, a few nanometers). For a sheet of length L and bending rigidity D, suspended in a fluid of

viscosity μ and subject to a uniform applied shear rate $\dot{\gamma}$, the ratio of viscous to bending forces can be estimated as

$$\frac{\text{“viscous forces”}}{\text{“bending forces”}} \sim \frac{\dot{\gamma}\mu L^3}{D}. \quad (1)$$

Large deformations are expected when this ratio is sufficiently large in comparison to a threshold value (which might depend weakly on the aspect ratio[19]) From this expression, it can be seen that the dependence on L of the non-dimensional bending rigidity is strong: a sheet of $L = 10$ nm is predicted to be 10^6 times less deformable, for a given $\dot{\gamma}$, than a sheet with $L = 1$ μm. In atomistic simulations, the sheets have L in the range of a few nanometers and therefore behave typically as nearly rigid sheets despite the large shear rates that are inherent in atomistic simulation approaches. Capturing the dynamics of relatively large sheets - the lateral size of graphene colloids can be several micrometers—requires mesoscopic or continuum simulation methods.

In the current work, we simulate the elastic sheets using a line-integral approach for Stokes. The formulation can be seen as a leading-order approximation to the Boundary Integral equations of Stokes flow for an elastic sheet in the limit of negligible sheet thickness. The formulation is described in detail, including formulation steps that are often superficially discussed in the literature. From the point of view of the discussion of the physics emerging from the simulations, the novelty of the work is twofold. First of all, we consider implications of our work for graphene dispersions, for ranges of parameters relevant to this application area. There are several publications on fluid-structure interaction with thin bodies (typically fibers) in the fluid mechanics literature, but these are typically motivated by understanding the mechanics of biological structures,[20,21] and it is not clear how the results could be applied to 2D nanomaterials. Second, we use the code to explore a range of dynamic morphologies that emerge when two sheets at close distance are exposed to a simple shear flow (i.e., a velocity field that varies linearly in one of the co-ordinate direction and contains a rotational component). The case of two particles at a close distance is particularly relevant to the dynamics of liquid-phase exfoliation and flow-induced deaggregation post stacking, and has not been considered in the fluid dynamics literature (previous work on parallel elastic fibers is relevant, but the range of distances considered is much larger than in the current work.[22])

Very recent simulations of single sheets in simple shear flow represents single sheets as a collection of beads, with hydrodynamic interactions based on Rotne–Prager–Yamakawa approximation accounting for the long-range hydrodynamic interactions between different elements of the sheet.[14] The line integral formulation of our method is based on discretizing a boundary integral equation, and includes both long-range and short-range interactions. Furthermore, our simulations are 2D while those in Ref. 14 are 3D. Relevant is also recent simulation work on elastic sheets in planar or biaxial extensional flows.[15] The main focus of that work was understanding the limit in which a sheet stretches without bound at a critical rate of extension. Besides the marked differences between particle dynamics in extensional and simple shear, stretching deformations are important for two-dimensional polymers, but only marginally for graphene and other 2D crystals due the very high tensile modulus these nanostructures display.

The current investigation has a practical motivation. The challenge of observing dynamic changes in the morphology of 2D nanosheets experimentally is remarkable. We are not aware of a single main-stream experimental technique that allows to access the deformation dynamics of single sheets in shear flow. Static techniques, such as Transmission Electron Microscope (TEM) and Scanning Electron Microscopy (SEM), are often used to characterize the morphology of 2D nanosheets[23,24] (in Fig. 1 we show highly deformed nanosheets from TEM images obtained by one of the authors with the experimental procedure described in Ref. 25). These techniques, however, provide only static information, and do not help explaining how complex nanosheet morphologies are obtained. We hope that our simulations will give insights useful for interpreting these experimental observations.

II. NUMERICAL MODEL

The simulations consider elastic sheets of length L and thickness $h \ll L$, immersed in an incompressible, unbounded fluid of viscosity μ. The model is two-dimensional, i.e., we represent each sheet by considering the dynamics of its cross section in the x–y (flow) plane. The undisturbed velocity field is denoted as $\mathbf{u}_\infty = \dot{\gamma} y \mathbf{e}_x$, where $\mathbf{e}_x$ is the unit vector along the x-coordinate parallel to the undisturbed flow. We neglect the inertia of each sheet and assume that the flow around each sheet is governed by the incompressible Stokes flow equations. These two assumptions hold well for small colloidal particles. The no-slip condition is assumed to hold at the solid-liquid boundary. The no-slip condition is often not satisfied by 2D nanomaterials,[26] but we make this assumption here for simplicity and as a model for all the cases in which the hydrodynamic slip length is smaller than the particle thickness (for a discussion of the limitations of this assumption for graphene and other 2D nanomaterials, see Refs. 2, 16, and 27). At the start of the simulation the sheet centers are located at (in the single-sheet case) or near (in the two-sheet case) the origin $x = 0, y = 0$.

A. Line integral formulation

Our numerical solution to the fluid structure interaction problem is based on a regularized Stokeslet approach whereby the regularized Stokeslet is applied at the centerline of the elastic body. This is an approximate model that has been employed with success in a variety

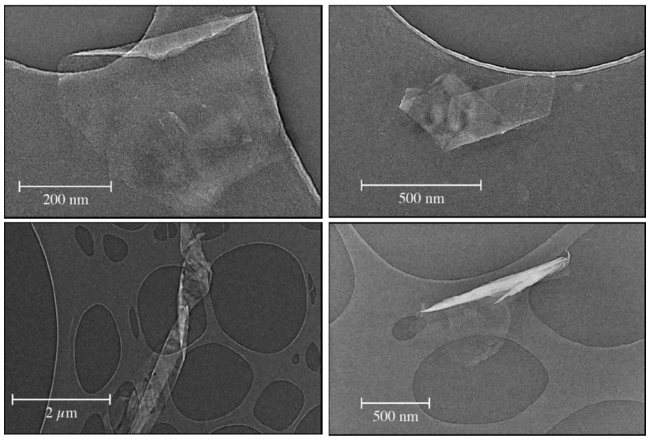

FIG. 1. Transmission electron microscopy images of folded graphene sheets following liquid-phase exfoliation of graphite in a Taylor–Couette apparatus (solvent: NMP; average shear rate $\langle\dot{\gamma}\rangle = 3.2 \times 10^4\ \text{s}^{-1}$).

of fluid-structure interaction problems.[20,21,28–30] The centerline approximation of the disturbance velocity produced by each sheet represents the leading-order approximation in a multipole expansion of the flow produced by the sheet and is conceptually similar to the approximation used, for example, in the slender body theory for rods.[31] We describe the formulation for a single body, detailing assumptions. The boundary integral representation of the Stokes equation for a body bounded by a line contour C is[32]

$$\mathbf{u}(\mathbf{x},t)=\mathbf{u}^{\infty}(\mathbf{x})-\frac{1}{4\pi\mu}\int_C \mathbf{G}(\mathbf{x},\mathbf{x_0})\cdot\mathbf{f}(\mathbf{x}_0)\mathrm{d}\ell(\mathbf{x}_0) +\frac{1}{4\pi}\int_C \mathbf{u}(\mathbf{x}_0)\cdot\mathbf{T}(\mathbf{x},\mathbf{x_0})\cdot\mathbf{n}(\mathbf{x}_0)\mathrm{d}\ell(\mathbf{x}_0). \tag{2}$$

Here, t is time, $\mathbf{n}$ is the unit normal to C pointing toward the interior of the body, $\mathbf{u}$ is the fluid velocity, $\mathbf{u}^{\infty}$ is the undisturbed fluid velocity (simple shear in our case), $\mathbf{f}=\boldsymbol{\sigma}\cdot\mathbf{n}$ is the hydrodynamic traction, and $\mathbf{G}$ and $\mathbf{T}$ are the Oseen tensors associated with the velocity and stress fields, respectively. The position vectors $\mathbf{x}_0$ and $\mathbf{x}_0$ are evaluated on the contour C and in the fluid region, respectively. The time dependence originates from the dependence of the domain of integration C on time.

Because we neglect the sheet's inertia, an exact balance holds between the total hydrodynamic traction on each small element of the sheet (including both sides of the sheet) and the internal elastic forces acting on that element. These latter are only a function of the configuration of the elastic body. If the second integral on the right-hand side (the double layer integral) was zero, one could update Eq. (2) in a step-by-step manner: calculate the sheet configuration, from the configuration calculate the traction, and from the boundary velocity calculate the new configuration. For a general deformable body, the double layer integral on the right-hand side of Eq. (2) is not zero. However, when the body is thin and inextensible, changes in thickness are negligible and one can assume $\int_C \mathbf{u}(\mathbf{x}_0)\cdot\mathbf{n}(\mathbf{x}_0)\mathrm{d}\ell(\mathbf{x}_0)\simeq 0$.[30] Under this approximation, Eq. (2) simplifies to[32]

$$\mathbf{u}(\mathbf{x},t)=\mathbf{u}^{\infty}(\mathbf{x})-\frac{1}{4\pi\mu}\int_C \mathbf{G}(\mathbf{x},\mathbf{x_0})\cdot\mathbf{f}(\mathbf{x}_0)\mathrm{d}\ell(\mathbf{x}_0). \tag{3}$$

In the classical boundary integral method, evaluation of this equation in the limit $\mathbf{x}\to\mathbf{x}_0$ together with the use of the no-slip boundary condition on C leads to an integral equation for $\mathbf{f}$. This approach requires the analytical integration of the singular kernel $\mathbf{G}$ over the discretization element.[32] While this is doable in 2D, it is much more cumbersome in 3D. As we seek an approach that could eventually be extended to complex and potentially multiparticle three-dimensional simulations, we discretize Eq. (3) by using a nonsingular kernel G^{ε}, parameterized on a regularization length ε.[29,33] The advantage of adopting a regularized Green's function is that the integral involving a nonsingular kernel can be discretized using standard formulas. We adopt a second-order mid-point approximation whether the point $\mathbf{x}_0$ coincides with $\mathbf{x}$ or not. The smoothing intrinsic in the adoption of a regularized kernel has also advantages in terms of numerical stability of the resulting code. In our implementation, we adopt the following regularized Green's function:[29]

$$G^{\varepsilon}_{jm}=\delta_{jm}\left(\log(R_0+\varepsilon)-\frac{\varepsilon(R_0+2\varepsilon)}{R_0(R_0+\varepsilon)}\right)-\frac{\hat{x}_j\hat{x}_m(R_0+2\varepsilon)}{R_0(R_0+\varepsilon)^2} \tag{4}$$

where we have used index notation for the Green function tensor and the position vectors; $\hat{x}_j=x_j-x_{0j}$ is the jth component of $\mathbf{x}_0-\mathbf{x}$ and $R_0=\sqrt{|\mathbf{x}-\mathbf{x}_0|^2+\varepsilon^2}$. In the limit $\varepsilon\to 0$, Eq. (4) recovers the (singular) 2D Green's function of Stokes flow.

We adopt a leading-order approximation for the line integral (3), in which the nonsingular kernel is evaluated at the centerline of the body. To see how the method works, consider the case illustrated in Fig. 2. In this example the body's centerline is straight. Evaluating the integral (3) on the upper surface $C^{+}=\{(s,h(s)/2)\}$ of the body gives

$$\begin{aligned}\mathbf{u}(s,h/2,t)-\mathbf{u}^{\infty}(s,h/2,t)&=-\frac{1}{4\pi\mu}\int_{s'=0}^{s'=L}\mathbf{G}^{\varepsilon}(s,h(s)/2;s',h(s')/2)\cdot\mathbf{f}(s',h(s')/2)dl\\&\quad-\frac{1}{4\pi\mu}\int_{s'=0}^{s'=L}\mathbf{G}^{\varepsilon}(s,h(s)/2;s',-h(s')/2)\cdot\mathbf{f}(s',-h(s')/2)dl\,,\end{aligned} \tag{5}$$

where s and s' are curvilinear coordinates along the centerline, the function $h(s)$ describes the thickness of the body and dl is an infinitesimal element of length. Because h is small, with an $O(h)$ error, we can approximate the Green's function as follows:

$$\mathbf{G}^{\varepsilon}(s,h(s)/2;s',h(s')/2)\simeq\mathbf{G}^{\varepsilon}(s,0;s',0), \tag{6}$$

$$\mathbf{G}^{\varepsilon}(s,h(s)/2;s',-h(s')/2)\simeq\mathbf{G}^{\varepsilon}(s,0;s',0). \tag{7}$$

Inserting these approximate expressions into (5) yields

$$\mathbf{u}(s,0,t)-\mathbf{u}^{\infty}(s,0,t)=-\frac{1}{4\pi\mu}\int_{s'=0}^{s'=L}\mathbf{G}^{\varepsilon}(s,0;s'0)\cdot\Delta\mathbf{f}(s')ds', \tag{8}$$

where $\Delta\mathbf{f}(s')=\mathbf{f}(s',h(s')/2)+\mathbf{f}(s',-h(s')/2)$ is the total force on the body (per unit length) on an element centered at s'; the fluid velocity has been evaluated, also with an $O(h)$ error, at the body's centerline. Also, to leading order $d\ell=ds'$ away from the edges. For a generally curved body, the procedure is the same, leading to

$$\frac{\partial\mathbf{X}}{\partial t}=\mathbf{u}^{\infty}(\mathbf{X})-\frac{1}{4\pi\mu}\int_{C_0}\mathbf{G}^{\varepsilon}(\mathbf{X}(s),\mathbf{X}(s'))\cdot\Delta\mathbf{f}(s')\mathrm{d}s', \tag{9}$$

where C_0 denotes the body's centerline. In this equation, we have used the no-slip condition to write $\partial(\mathbf{X}(s,t))/\partial t=\mathbf{X}((s),t)$. If the force density $\Delta\mathbf{f}$ can be expressed in terms of the centerline shape $X(s,t)$, Eq. (9) can be marched numerically in time to find the centerline position at each time step.

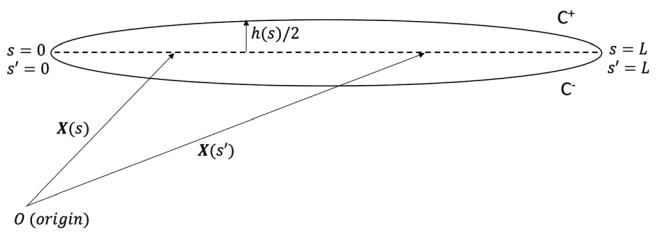

FIG. 2. Parameterization of the integral for a straight body of thickness h. The domain of integration C is composed of an upper surface C^{+} and a lower surface C^{-}, located symmetrically about the centerline position $\mathbf{X}(s)$.

The regularized Stokes approach with a centerline approximation has been shown to lead to accurate 3D solutions of a sheet moving according to an assigned kinematics.[30] Here instead the motion of the centerline is not assigned, but is governed by the system of forces acting on the elastic body. Equation (9) is valid provided that h is much smaller than the minimum radius of curvature of the centerline. Higher-order approximations are possible retaining more terms in the Taylor expansion for the Green's function.

B. Closure between hydrodynamic and elastic forces

To update Eq. (9), it is necessary to relate $\Delta\mathbf{f}$ to the configuration of the sheet. A thin flexible sheet in a shear flow is subject to a normal hydrodynamic traction from the fluid "pushing" onto the slender surface of the sheet. Since these stresses act in the normal direction to the surface, they can be assumed to be independent of the thickness h of the sheet. The nanosheet will also experience tangential traction over its boundary that scale with the thickness of the sheet.[34] There will be two components due to the tangential traction. One is a shearing component which translates into a line distribution of couples on the sheet. This term is proportional to h.[34] The second component instead produces an axial force on the sheet. This term is independent of h in the limit $h/L \to 0$. For thin sheets the axial and normal forces are much greater than the tangential force and any contribution from the hydrodynamic force on the edges provided that the sheet is not flat and perfectly aligned with the flow.[34] In our model, since we are interested in understanding the dynamics when the sheet deformations are large, then the tangential and edge forces will be neglected (a study of edge and tangential shearing effects is presented in Ref. 2; for the effect of edges on hydrodynamic peeling and sliding of graphene sheets, see Refs. 35 and 36). Given the elastic energy of the body at a certain time, $\mathscr{E}(\mathbf{X}, t)$, the force exerted by the body on the fluid can be calculated. Retaining only the normal total traction and the axial force, we can derive from the bending and tension of the central line according to

$$\mathbf{F} = -\frac{\partial \mathscr{E}}{\partial \mathbf{X}}. \tag{10}$$

where $\mathbf{F} = \Delta\mathbf{f}\, w\, \mathrm{d}s$ is the total hydrodynamic force on an element of length $\mathrm{d}s$ and width w (this last quantity will drop out from the calculations, but we retain it to avoid confusion regarding the meaning of "force per unit length"). The elastic energy can be decomposed into a tensile component and a bending component as $\mathscr{E} = \mathscr{E}_S + \mathscr{E}_B$. The tensile (stretching) and bending components are given, respectively, by[20,29,37]

$$\mathscr{E}_S = \frac{1}{2} Kw \int_L \left(\left| \frac{\partial \mathbf{X}}{\partial s} \right| - 1 \right)^2 \mathrm{d}s, \tag{11}$$

$$\mathscr{E}_B = \frac{1}{2} Dw \int_L (\kappa(s))^2 \mathrm{d}s, \tag{12}$$

where $\kappa(s)$ is the curvature of each sheet and s is the curvilinear coordinate. The parameters K (Nm^{-1}) and D (Nm) are the tensile and bending rigidities of the sheet, respectively.

C. Implementation and validation

Each sheet is discretized into N points of coordinates $\mathbf{X}_i(t)$. The nodes are connected by springs with spring constant k_S that resist compression and extension of the sheet. Bending forces are accounted for by implementing rotational springs on each node, with spring constant k_B.[20,37]

The discretized stretching energy at a fixed time is given by

$$\mathscr{E}_S \simeq \frac{1}{2} \sum_{i=1}^{N-1} k_S (|\mathbf{X}_{i+1} - \mathbf{X}_i| - l_0)^2, \tag{13}$$

where l_0 is the length of the springs at rest. The corresponding bending energy is

$$\mathscr{E}_B \simeq \frac{1}{2} \sum_{i=1}^{N-2} k_B (|\mathbf{X}_{i+1} - \mathbf{X}_i||\mathbf{X}_i - \mathbf{X}_{i-1}| \sin\theta_i)^2, \tag{14}$$

where θ_i is the angle between two consecutive segments. For (13) and (14) to recover Eqs. (11) and (12) in the continuum limit $l_0/L \to 0$, k_S and k_B are given by $k_S = Kw l_0^{-1}$ and $k_B = Dw l_0^{-5}$.[20] The discretized traction $\Delta\mathbf{f} = \mathbf{F}/(l_0 w)$, calculated by taking the derivative of the discretized energies, is inserted into Eq. (9) to obtain

$$\frac{\partial \mathbf{X}_i}{\partial t} = \mathbf{u}^\infty(\mathbf{X}_i) + \frac{1}{4\pi\mu} \int_L \mathrm{d}\ell\, \mathbf{G}^\varepsilon \cdot \left[\frac{K}{2l_0^2} \frac{\partial}{\partial \mathbf{X}_i} \left(\sum_j \left(|\mathbf{X}_{j+1} - \mathbf{X}_j| - l_0 \right)^2 \right) \right] + \frac{1}{4\pi\mu} \int_L \mathrm{d}\ell\, \mathbf{G}^\varepsilon \cdot \left[\frac{D}{2l_0^6} \frac{\partial}{\partial \mathbf{X}_i} \left(\sum_j \left(|\mathbf{X}_{j+1} - \mathbf{X}_j||\mathbf{X}_j - \mathbf{X}_{j-1}| \sin\theta_j \right)^2 \right) \right]. \tag{15}$$

This equation is marched in time with an explicit Euler method to find the new sheet configuration.

The accuracy of the code has been verified by considering the relaxation of a sheet presenting an initial sinusoidal perturbation in the absence of an external flow. Consider a sheet initially oriented in the x direction, immersed in a fluid at rest. If a small initial perturbation in the y direction is considered, the displacement of the plate can be parametrized by a function $\xi(x)$. For $|\nabla\xi| \ll 1$, the traction forces are directed in the y-direction and are given by $f_y(x) = D\partial^4\xi/\partial x^4$. For small vertical displacements, the 2D Green's function can be approximated as

$$\mathbf{G} = \begin{pmatrix} -\ln|x - x_0| + 1 & 0 \\ 0 & -\ln|x - x_0| \end{pmatrix}. \tag{16}$$

Thus, Eq. (9) reduces to

$$\frac{\partial \xi(x_0)}{\partial t} = \frac{1}{4\pi\mu} \int_L \ln|x - x_0| D \frac{\partial^4 \xi}{\partial x^4} \mathrm{d}x. \tag{17}$$

This equation can be readily solved by Fourier transform in the limit $L \to \infty$ to obtain a differential equation for each Fourier component $\hat{\xi}(k)$:

$$\frac{\partial \hat{\xi}(k)}{\partial t} = -\frac{Dk^3}{4\mu} \hat{\xi}(k). \tag{18}$$

(The Fourier transform gives also delta function term, but this is zero on account of the fact that the total force on the sheet is zero for a non-inertial particle not acted upon by external forces.[38]) Thus, a sinusoidal deformation should decay exponentially with a decay constant $T_k = 4\mu/(Dk^3)$. Figure 3 compares simulation results for an initial sinusoidal perturbation of wavenumber $k = 2\pi$ and amplitude

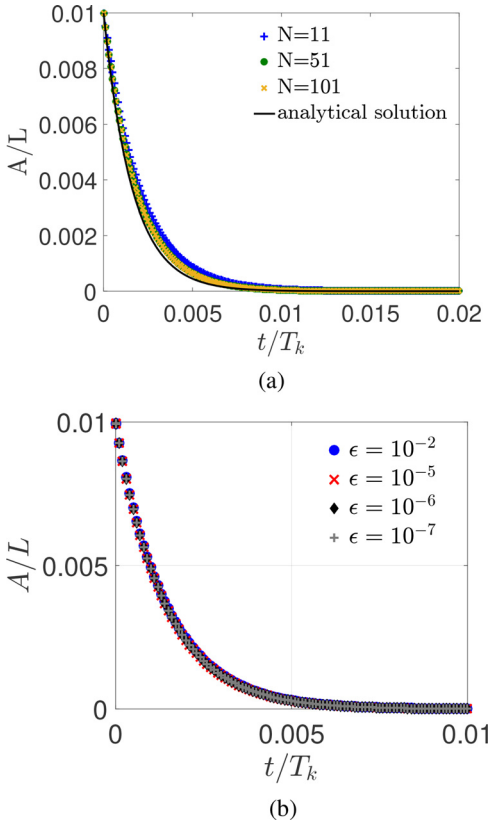

FIG. 3. (a) Relaxation of the displacement amplitude $A(t)$ for different discretization point numbers N. The numerical results approach the analytical solution as N increases. (b) Relaxation of the displacement amplitude $A(t)$ for different values of the regularization parameter ε.

$A_0/L = 0.01$ with the analytical solution, for different numbers of discretization points N. As shown in Fig. 3(a), the numerical results approach the analytical solution as N increases. In our simulations, we use $N = 51$ as a good compromise between accuracy and speed of the code.

The parameter ε in the regularized Stokeslet is usually chosen to be of the order of the radius of the rod (for 1D bodies such as flagella[29]) or the thickness of the sheet in the case of 2D particles.[30] This choice has been applied in particular, for bodies with moderately small aspect ratio ($\varepsilon \sim 10^{-1}$–10^{-2}). In our test for extremely thin particles such as nanosheets for which a typical value is $\varepsilon \sim 10^{-3}$, the regularization parameter does not influence the relaxation dynamics, as shown in Fig. 3(b). The code sensitivity test to the parameter ε has been performed with the same initial configuration used in the code validation paragraph: a sinusoidal displacement with $A_0/L = 10^{-2}$ and $k = 2\pi$ is applied to a sheet immersed in a quiescent fluid with $T_k = 1/(20\pi^3)$. As shown in Fig. 3(b), the exponential relaxation does not show a significant dependency on ε. In the simulations presented in Sec. III, the value $\varepsilon = 10^{-6}$ was used.

To further validate our code, the rotational dynamics of a rigid sheet initially oriented at an angle of 6° with respect to the undisturbed flow direction [$\theta = -84°$ with respect to the flow normal, see inset of Fig. 4(a)] is compared against Jeffery's analytical solution. The rigidity constraint is obtained by setting the non-dimensional tensile and bending rigidity parameters to large values. Parameters that are varied are the number of discretization points N [Fig. 4(a)] and the value of the regularization parameter ε [Fig. 4(b)]. The comparison with Jeffery's solution $\theta(t) = \arctan(\dot{\gamma}t)$,[39] valid for $h/L \to 0$, is excellent for the values of N and ε considered.

III. RESULTS

In Secs. III–V, we analyze simulations considering either a single sheet or two sheets initially parallel at close separation d_0. The dimensional parameters appearing in Eq. (9) with the closure given by Eq. (10) are $\dot{\gamma}$, D, K, μ, and L, the latter variable appearing in the domain of integration. The initial condition in the two-sheet simulation also

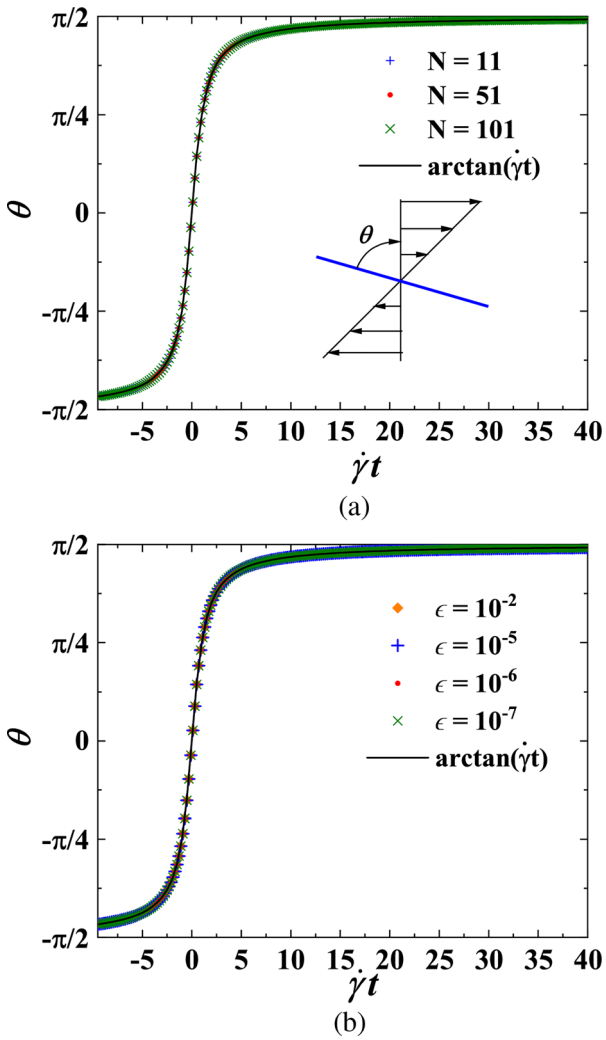

FIG. 4. Rotational dynamics of a rigid sheet in a shear flow compared to the analytical solution of Jeffery's orbit for an initial angle different from zero: (a) different numbers of discretization points N, and (b) different values of the parameter ε. Note that the origin of the horizontal axis is chosen so that $\theta = 0$ (particle oriented perpendicular to the flow) when $t = 0$.

introduces the extra length scale d_0. With these, we can construct three non-dimensional parameters governing the dynamics of the sheets: the ratio of viscous and bending forces,

$$\hat{\dot{\gamma}}_L = \frac{\mu \dot{\gamma} L^3}{D}, \tag{19}$$

the ratio of viscous and tensile forces,

$$\hat{K} = \frac{\mu \dot{\gamma} L}{K}, \tag{20}$$

and d_0/L. Graphene and other 2D nanomaterials have very large in-layer strength (of the order of ~100 GPa and more[40]) hence typically $\hat{K}$ is so small to be unimportant in controlling the rotational and deformation dynamics.[15] In all our simulations, we therefore set $\hat{K} = 10^{-3}$. Thus, the important parameters are the elasto-viscous number $\hat{\dot{\gamma}}_L$ and d_0/L, the single-particle dynamics corresponding to $d_0/L \to \infty$.

We prescribe an initial shape perturbation, which can be either sinusoidal (odd perturbation of the form $\xi = a_0/L \sin(2\pi x/L)$ with $0 \le x \le L$) or following a cosine function (even perturbation of the form $\xi = -a_0/L \cos(2\pi x/L)$). The use of such perturbation was found necessary in both the single- and two-particle simulations (this feature is intrinsic in methods that neglect the thickness and the accompanying tangential and edge forces[14]) and characterizes many published simulations of fibers, see Ref. 41 for example. In single particle simulations, an initial inclination angle was also found necessary to observe a rotational dynamics. This behavior can be understood from the following considerations. A simple shear flow can be decomposed into a pure rotation and a bi-axial extensional flow. The latter is characterized by a compressional and extensional axis, which for our case are oriented as in Fig. 5(a). If a straight sheet is considered, the second integral in Eq. (15), which represents the velocity perturbation by bending forces, is exactly zero. In this case, the sheet velocity is given by the sum of the background velocity and the velocity due to the tensile traction forces. For a straight sheet oriented along the undisturbed flow, the tensile forces are also parallel to the undisturbed flow, hence the sheet does not rotate. This occurs because of the assumption of no tangential and edge forces. If an inclined but initially straight sheet is considered, the integral associated with the bending force is zero, and again only the tensile traction forces act on the sheet tangentially. The background flow is parallel to the undisturbed flow and, combined with the tangential tractions, causes a convective velocity always perpendicular to the sheet and varying linearly along the sheet length [see Fig. 5(b)]. The resulting motion is therefore a pure rotation without bending. Finally, if a shape perturbation is prescribed without an initial inclination, the perturbation decays before the sheet begins the rotational dynamics, and again the sheet rotates as a perfectly straight sheet.

We first consider a single sheet initially oriented at a small angle, $\pi/30$, for $\hat{\dot{\gamma}}_L = 100$. The initial deformation is sinusoidal with amplitude $a_0/L = 10^{-3}$. As can be seen in Fig. 6(a), the body deforms into an "S" shape when approaching the compressional axis of the flow. The sheet continues to rotate, reaching a maximum deformation when the average sheet orientation is roughly along the direction perpendicular to the flow, where the hydrodynamic force normal to the sheet is greatest. As the sheet crosses the extensional axis of the flow, it relaxes to a straight shape.

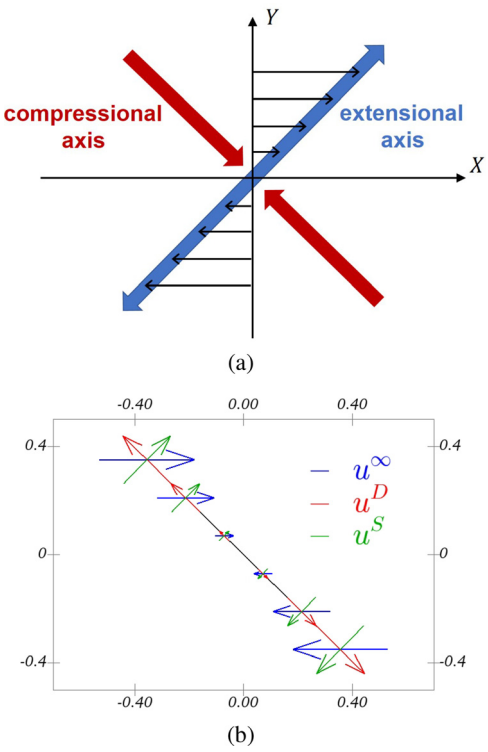

FIG. 5. (a) A simple shear flow can be decomposed into a purely rotational flow and an extensional flow with extensional and compressional axes oriented as in the figure (b) Background velocity $\mathbf{u}^\infty$, disturbance velocity $\mathbf{u}^D$ and total velocity $\mathbf{u}^S = \mathbf{u}^\infty + \mathbf{u}^D$ along an initially straight sheet. The velocities are plotted every ten discretization points.

In Fig. 6(b), we compare the shape evolution of two sheets being characterized by two different perturbation amplitudes $a_0/L = 10^{-2}$ (black line) and $a_0/L = 10^{-3}$ (red line). We fix $\hat{\dot{\gamma}}_L$ to a relatively large value, $\hat{\dot{\gamma}}_L = 1000$, to make the difference between the two cases more evident in the figures. The sheet with larger initial perturbation (black line) deforms faster than the red sheet and bends into an "S" shape [Fig. 6(b), $t\dot{\gamma} = 5$]. This shape is maintained by the black sheet at all times, while the red sheet shows signature of a large-deformation mode whereby the curvature of the sheet changes more than two times along the length of the sheet (see, e.g., the red sheet in the panel corresponding to $t\dot{\gamma} = 7$). As the sheets approach the extensional axes of the flow, the shapes of the two sheets become practically identical near the midpoint of the sheets. Interestingly, when the black sheet is aligned along the compressional axis it temporarily deforms without rotating. This feature occurs also for the red sheet, but the effect is less evident in this case.

In Fig. 7(a), we consider the case $\hat{\dot{\gamma}}_L = 2000$ and an initial orientation closer to the compressional axis of the shear flow. Because $\dot{\gamma}_L$ is larger than in Fig. 4(b), the amplitude of the sheet deformation is significantly more pronounced, particularly in the first part of the rotation. When the sheet orientation approaches the extensional axis, the sheet again relaxes to an "S" shape. Importantly for our later discussion on the possibility of self-adhesion, the minimum radius of curvature is seen to be smaller in Fig. 7(a) than in Fig. 6(b).

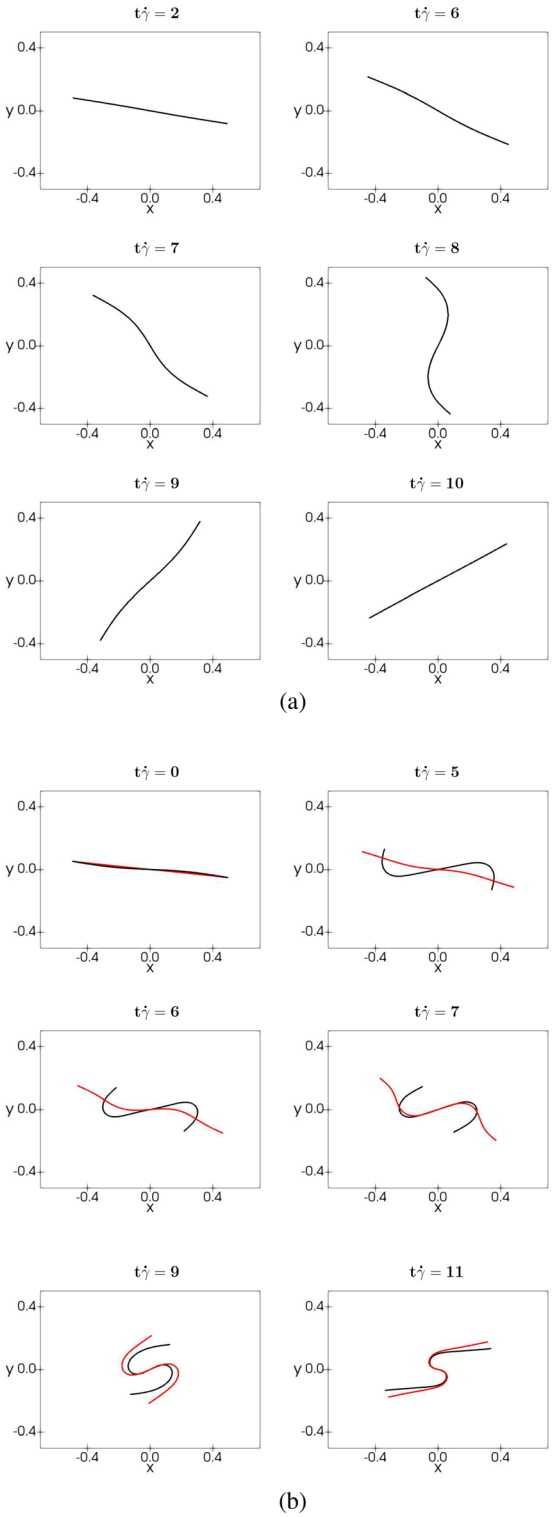

FIG. 6. (a) Single sheet dynamics for $\hat{\dot{\gamma}}_L = 100$ and an initial sinusoidal perturbation with $a_0/L = 10^{-3}$. (b) Shapes of identical sheets subject to different initial perturbations: $a_0/L = 10^{-2}$ for the black line and $a_0/L = 10^{-3}$ for the red line.

Figure 7(b) considers an even (cosinusoidal) initial perturbation while the non-dimensional shear rate is the same as in Fig. 7(a) ($\hat{\dot{\gamma}}_L = 2000$). With a cosine perturbation and at this non-dimensional shear rate, the sheet rolls onto itself, producing a characteristic "C" shape. The minimum distance between different parts of the sheet is smaller than in Fig. 7(a), despite the identical value of $\hat{\dot{\gamma}}_L$. If a lower non-dimensional shear rate is considered, the sheet dynamics is similar to Fig. 7(b), except that the "C" is less flattened (i.e., the radius of curvature of the fold is larger).

The simulations illustrate that the single-sheet dynamics is essentially characterized by three recurring deformation modes: the "S" shape, the "C" shape, and a deformation mode with more than two changes in curvature along the length of the sheet. Depending on the initial perturbation and on the flexural rigidity of the sheet, the sheet assumes one of these shapes while rotating. These deformation modes have been observed in experiments[42] and simulations[22,37,41,43] of flexible fibers.

It is of interest to compare the critical shear rate for flow-induced shape instability of rods and sheets (here we use the name "sheets" as a shorthand for plates, flakes or any disk-shaped particle). For both shapes, the axial compressive force produced by the fluid when the particle is oriented along the compressional axis is $\sim \mu a^2 c$, where $a = L/2$ is the semi-length of the body and c is at most a weak function of the aspect ratio (for rods, c depends logarithmically on the aspect ratio;[41,44] for thin oblate spheroids, an approximate expression for the critical buckling threshold derived by Lingard and Whitmore[44] assuming a purely axial hydrodynamic load model is consistent with $c = (3/\pi)10.36(1 - \frac{3\pi}{4}\alpha)$, where α is the small aspect ratio). When this axial hydrodynamic force becomes equal to a structural instability threshold of the order of $\sim B/a^2$ a (large-deformation) shape instability sets in[42,45]; here $B \propto Da$ is the total bending rigidity, i.e. the total bending moment on the structure per unit curvature. These estimates demonstrate that for both sheets and disks the critical shear rate to observe large deformations (deformation amplitude comparable to L) is

$$\dot{\gamma}_{critical} \sim \frac{B}{a^4}\frac{c}{\mu}. \tag{21}$$

For sheets, $B \propto Eab^3$, where E is the Young modulus and b the half-thickness; thus $\dot{\gamma}_{critical}$ has the same scaling with L as in Eq. (19). For rods, B is instead proportional to Eb^4 (e.g., for a rod of circular cross section of radius b, $B = (\pi/4)Eb^4$). Thus, for a given aspect ratio, and neglecting the weak dependence on c, the critical shear rate for a sheet is approximately $O(a/b)$ larger than the critical shear rate for a rod. The higher likelihood of observing fiber bending due to lower thresholds may be one of the explanations for why bending of fibers has been studied more extensively than bending of disks or other plate-like particles.

We now turn to two particle ("two-sheet") simulations. In our investigation we have explored a range of initial distances: $d_0/L = 0.1$, 0.05, and 0.01. We here report some of the most representative results. Unless specified, the sheet pairs are initially aligned with the flow and an initial shape perturbation is applied.

Figure 8(a) shows the pair dynamics in the case $\hat{\dot{\gamma}}_L = 10$. The initial sinusoidal sheet perturbation (we use $a_0/L = 0.05$) quickly relaxes and the sheets become practically flat already at $t\dot{\gamma} = 5$. The subsequent motion consists essentially of a rigid rotation of the pair, until both sheets align in the flow direction. At this orientation, the sheets

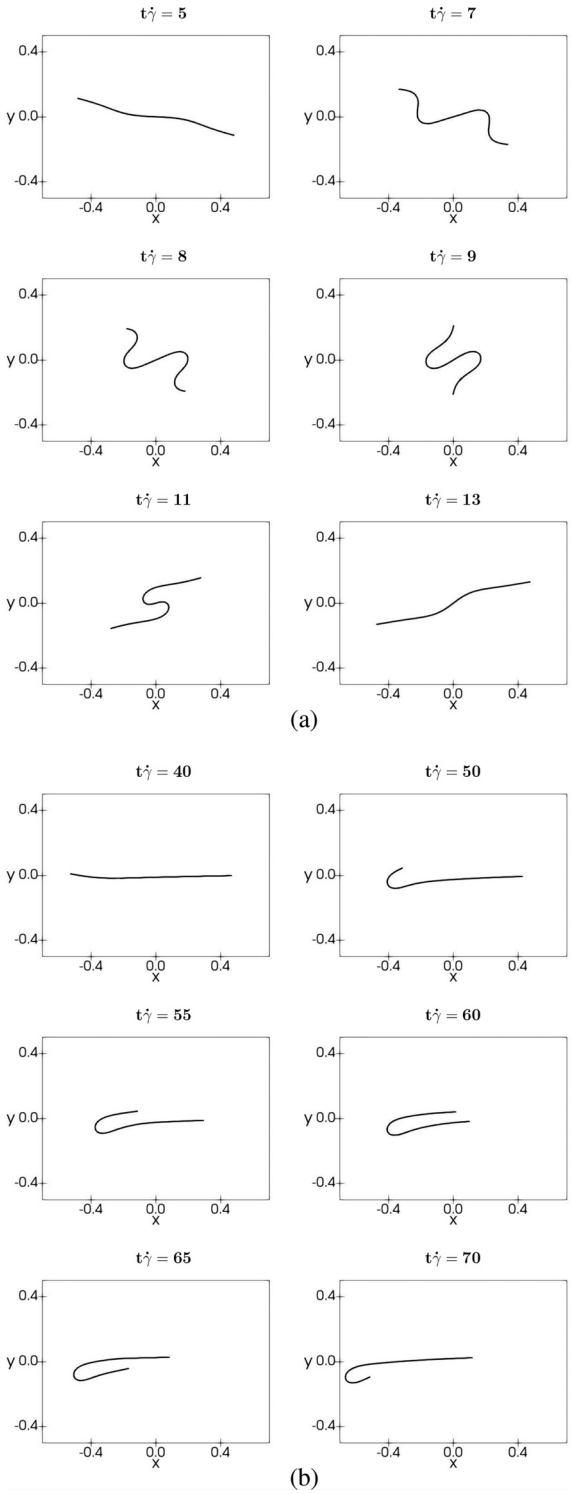

FIG. 7. (a) Single sheet dynamics. Deformation mode with more than two changes in curvature along the length of the sheet for $\hat{\gamma}_L = 2000$. (b) "C" shape deformation of a sheet with an initial even perturbation and $\hat{\gamma}_L = 2000$. For a video of the simulations, see supplemenatry material.

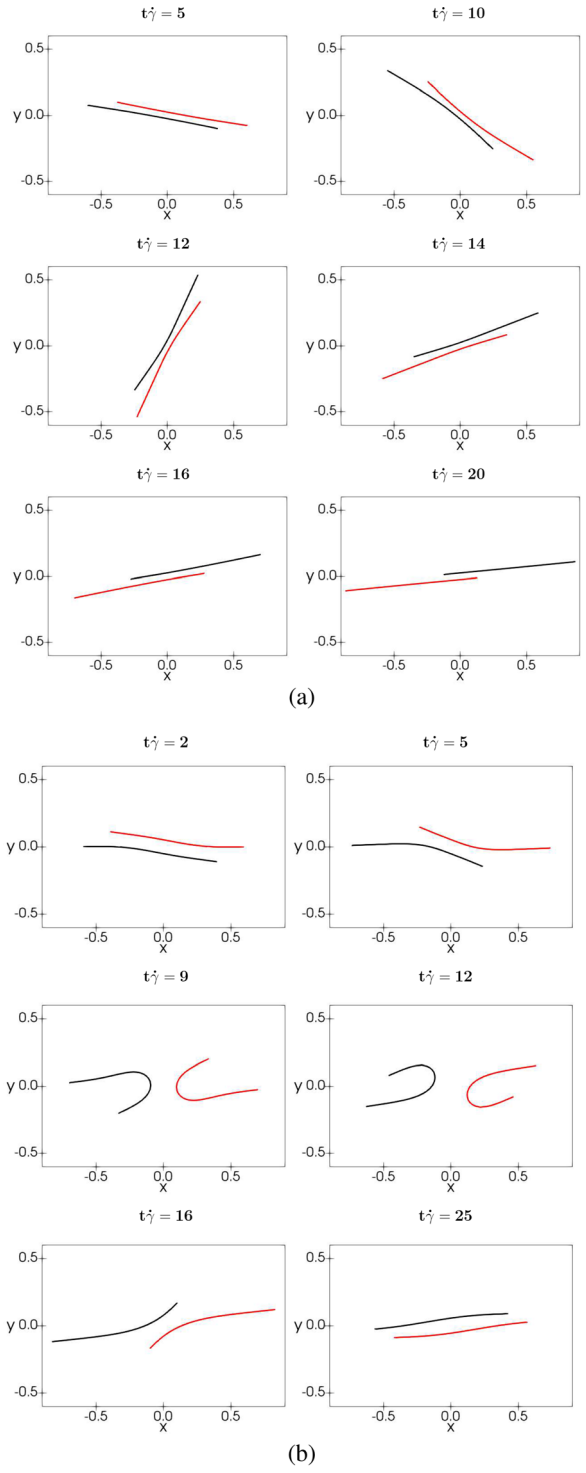

FIG. 8. (a) Dynamics of two moderately rigid sheets ($\hat{\gamma} = 10$) for $d_0/L = 0.05$, showing a rotational motion and a sliding detachment without strong bending of the sheets. The initial perturbation is sinusoidal with $a_0/L = 0.05$. (b) Deformation of and hydrodynamic interaction between two sheets with an initial odd perturbation ($a_0/L = 0.005$), initial distance $d_0/L = 0.1$ and $\hat{\gamma}_L = 100$.

slide with respect to each other without bending, maintaining an orientation nearly parallel to the undisturbed streamlines.

One might wonder why for $\hat{\dot{\gamma}}_L = 10$, which is significantly larger than 1, the sheets still behave as rigid elements. This apparent inconsistency can be explained by considering a better approximation of the respective orders of magnitude of the viscous and bending forces, obtained by using the semi-length $a = L/2$ instead of L. A non-dimensional shear rate of 10 based on L corresponds to a non-dimensional shear rate based on a of $10/8 = 1.25$, which is $O(1)$ as expected. Of course, whether the length or the semi-length is chosen is unimportant, as long as it is understood that a value of $\hat{\dot{\gamma}}_L = 10$ is not large as far as flexibility is concerned.

In Fig. 8(b), we consider two sheets for $\hat{\dot{\gamma}}_L = 100$. The sheets are initially parallel and separated by a distance $d_0/L = 0.1$. A sinusoidal perturbation of amplitude $a_0/L = 0.05$ is imposed. After an initial sliding motion, the sheets deform into mirror-symmetric "C" shapes (the sheets deform into a "C" shape even if their initial shape is sinusoidal, unlike for the single-sheet case). During the deformation, the minimum separation first increases and then decreases. For $t\dot{\gamma} = 25$, the sheets have reached approximately the initial separation. We call this dynamics "sheet reassembly."

If the non-dimensional shear rate is increased to $\hat{\dot{\gamma}}_L = 1000$, the sheet dynamics becomes more complex, with different bending modes occurring at different times [Fig. 9(a)]. At the initial stages of the dynamics, the particles assume an "S" shape. Afterward they display deformation with more than two curvature changes ($t\dot{\gamma} = 6.5$) along the length of the sheet. Later they assume a "C" shape ($t\dot{\gamma} = 10$), before finally relaxing to a straight shape ($t\dot{\gamma} = 15$). Although the initial inter-particle distance and the initial perturbations are the same as in Fig. 8(b), in Fig. 9(a) the minimum distance between the sheets remain roughly comparable to the initial distance at all times (in Fig. 8 the minimum distance increases significantly at intermediate times).

If smaller initial distances are considered, $d_0/L = 0.01$, the lubrication forces between shape-conforming sheets keep the sheets adhered to each other for relatively long times [Fig. 9(b)]. Normal lubrication forces between two two-dimensional parallel sheets of finite length L located at a distance d scale as $F_{\text{lub}} \sim \frac{\mu L^4}{d^3}\dot{d}$, where $\dot{d}$ is the separation velocity.[46] Because $d/L \ll 1$, this scaling corresponds to small normal velocities of the order of $\sim \frac{d^3}{L^2}\dot{\gamma}$ when the outer portion of the sheet pair is subject to a force $\sim \mu\dot{\gamma}Lw$.

In Fig. 9(b), we show the dynamics of two sheets for $\hat{\dot{\gamma}}_L = 2000$ and an even initial perturbation. The initial separation is $d_0/L = 0.01$, one tenth of that in Fig. 9(a). When the sheets are approximately straight ($t\dot{\gamma} \leq 25$), the overlap between the sheets decreases in time as the two sheets slide past each other. However, for $t\dot{\gamma} = 35$ the end of one of the two sheets curves following the vorticity of the undisturbed flow, forming a fold that "shields" the other sheet from the influence of the external flow. The second sheet thus experiences a weaker interaction with the external flow than in the initial stages of the dynamics, and its motion can be plausibly considered to be mainly controlled by the close-ranged hydrodynamic interaction with the first sheet.

In liquid-phase exfoliation for the production of graphene from graphite particles, the microscopic exfoliation is thought to be caused in part by the "peeling" of single or few-layer graphene sheets from a relatively rigid mother particle.[12,35] To model this situation, in Fig. 10(a) we prescribe an initial shape resembling a lifted flap to one of the sheets (the "upper" sheet), as done in Ref. 35. Furthermore, to model

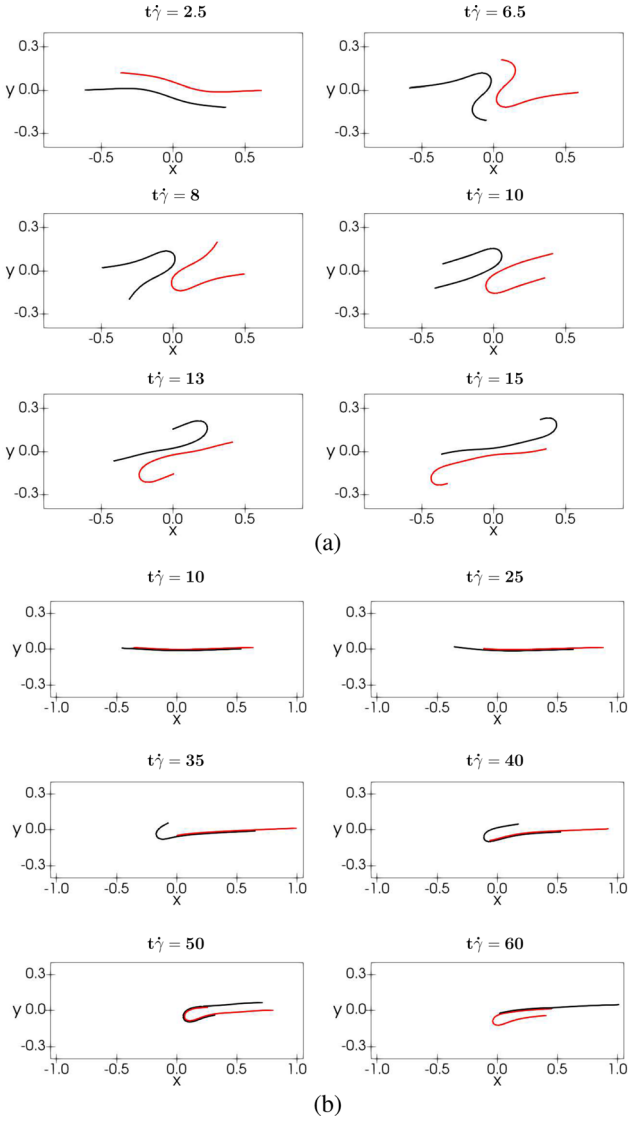

FIG. 9. (a) Interaction between two sheets for an initial odd perturbation ($a_0/L = 0.05$), initial distance $d_0/L = 0.1$ and $\hat{\dot{\gamma}}_L = 1000$. (b) Initial even perturbation ($a_0/L = 0.05$), initial distance $d_0/L = 0.01$ and $\hat{\dot{\gamma}}_L = 2000$. For a video of the simulations, see supplementary material.

the larger rigidity of a mother particle, we prescribe for the upper sheet a value of $\dot{\gamma}_L$ ten times larger than that of the lower sheet.

In Fig. 10(a), the presence of the flap favors a dynamics in which the upper sheet bends while the lower sheet barely deforms initially. The dynamics resembles, qualitatively, that of classical peeling, well studied in solid mechanics, which is based on a competition between bending forces and short-range adhesion forces (due, e.g., to van der Waals interactions). Normal lubrication forces depend on separatation distance [$d(t)$] and relative velocity of separation ($\dot{d}$) between adjacent surfaces. Conservative adhesion forces depend only on relative distance. However, the two forces can lead to qualitatively similar dynamics if the external force causing peeling is applied on a relatively fast

timescale. Consider, for example, two initially bonded sheets, completely immersed in a liquid (a configuration examined experimentally in Ref. 46). An edge force is applied to one of the edges of the upper sheet while the lower sheet is stationary. Assume that lubrication forces are the only resistive forces acting on the top sheet. If the external edge force is applied quasi-statically, or very slowly, the shape of the upper sheet has time to relax to a straight shape. However, if the edge force was applied on a short timescale, the edge would peel off first, bending the sheet, while a portion of the deformable sheet would be kept "glued" to the stationary sheet by lubrication forces. This example suggests a qualitative analogy between peeling with lubrication forces and peeling with conservative adhesion forces depending on a suitably defined elasto-viscous response time.[46] In our case, the timescale of the external forces is likely to be $\dot{\gamma}^{-1}$, as this is the time that defines the external flow field.

Finally, Figure 10(b) illustrates the dynamics of two extremely flexible sheets ($\hat{\dot{\gamma}} = 2000$) for $d_0/L = 0.01$ and an even initial perturbation. For this small separation, the hydrodynamic interaction between the sheets forces the two particle to move almost as a single, compound body. The hydrodynamic interaction change the tendency of the sheets to bend in an even or odd mode. Indeed, the initial even perturbation evolves into a complex deformation mode with more than 2 change in curvature and then into an (odd) "S" shape.

IV. DISCUSSION

The single-sheet simulations result indicate a strong dependence of the deformation and rotational dynamics on the initial conditions: small changes in the initial shape of the sheets can lead to significantly different time evolutions (Fig. 6). The sensitivity to the initial conditions makes it difficult to define precise ranges of $\hat{\dot{\gamma}}_L$ corresponding to different dynamical behaviors. In our simulations, marked deformations with evident "S," "C" or complex buckling shapes with a characteristic curvature $\sim 1/L$ become apparent for a critical value of the elasto-viscous number $\hat{\dot{\gamma}}_L \simeq 100$. Growing curvatures $\ll 1/L$ are already noticeable for $\hat{\dot{\gamma}}_L \sim 10$. For comparison, the buckling threshold for rods is $\hat{\dot{\gamma}}_L = \frac{153.48}{8\pi} c$, where $c = -\ln(\alpha^2 e)$ with e the Euler constant and α the aspect ratio;[47] this expression gives $\hat{\dot{\gamma}}_L = 78.0$ and $\hat{\dot{\gamma}}_L = 163.4$ for $\alpha = 10^{-3}$ and $\alpha = 10^{-6}$, respectively. Our line integral formulation with the 2D regularized Green's function is not identical to the formulation for 3D rods, but we observe that a threshold of $\hat{\dot{\gamma}}_L \sim 100$ is not incompatible with the prediction for rods having an aspect ratio of the order of the regularization parameter used in the current work ($\varepsilon = 10^{-6}$).

The buckling dynamics in a simple shear flow of a hexagonal disk modeled as a collection of beads interacting via long-range hydrodynamic interactions has been recently simulated.[14] In that work, a prediction of the critical shear rate for buckling based on a linear stability analysis of an Euler beam model was developed. In the model, the true hydrodynamic stress on the structure was approximated with the undisturbed hydrodynamic stress. Despite its simplicity, the model showed a good agreement with the simulation. It predicted a first buckling mode for a non-dimensional number $S = \kappa/(\pi\mu\dot{\gamma}R^3)$ of about 5×10^{-3}, where $\kappa = Eh^3/(12(1-\nu^2))$, E is the effective Young modulus of the material, ν is the Poisson ratio, and R is the circumradius of the hexagonal sheet. To compare their 3D results to our 2D model, we need to translate the bending rigidity parameter from 3D to 2D. To do so, we use the relation $B = 2RD = E\frac{1}{6}Rh^3$ obtained assuming that the cross section of the sheet is a rectangle of width equal to the diameter $2R$ and height h. With this relation, $S \approx 5 \times 10^{-3}$ corresponds to $\dot{\gamma}_L \simeq 500$, slightly larger than what we observe but of the same order of magnitude (for this calculation, we have assumed an incompressible material, for

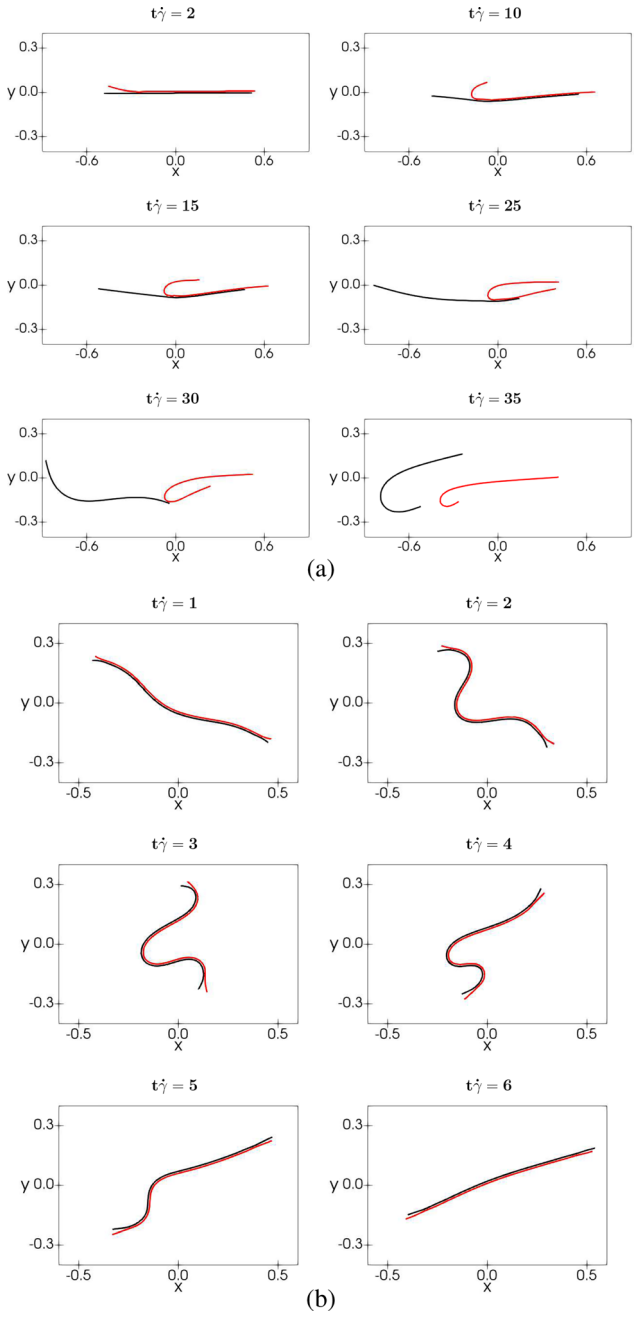

FIG. 10. (a) Peeling-like dynamics of two sheets with different bending stiffness ($\hat{\dot{\gamma}}_L = 1000$ for the upper sheet; $\hat{\dot{\gamma}}_L = 10^2$ for the lower sheet). The initial minimum distance between the sheets is $d_0/L = 0.01$. (b) Flexible sheets ($\hat{\dot{\gamma}} = 2000$) with an even initial configuration.

which $\nu^2 \ll 1$). A semi-analytical result for the buckling threshold of disks was derived by Lingard and Whitmore[44] to model the buckling of red blood cells in shear flows. In this work, the exact hydrodynamic surface stress on an ellipsoid was used to estimate the hydrodynamic load on the disk. For slender disks, this analysis predicts $\mu\dot{\gamma}_c \simeq 10.36\frac{4}{\pi}E\frac{h^3}{L^3}$. Using for D the expression mentioned above, we get $\hat{\dot{\gamma}}_L \simeq 158$, very close to our numerical prediction. While we are not aware of direct experimental measurements of buckling of very thin, flexible plate-like particles, in rheological experiments with plate-like nanocrystals suspended in a Newtonian epoxy, White *et al.*[45] noticed a weak maximum in the flow curve relating viscosity and shear rate. The maximum in the flow curve corresponded to shear rates comparable to those predicted by the semi-analytical expression of Lingard & Whitmore. This induced the authors to argue that flow-induced buckling played a role in increasing the viscosity, although the exact mechanism were only speculated about. In summary, all analytical and simulation data published so far, as well as our data and scaling estimates, and one recent rheological measurement, seem to point to a buckling threshold governed by expression (21) with c a constant of order 1. Incidentally, this demonstrates that for plate-like particles using the plate radius (and not the diameter) in scaling arguments to estimate viscous and bending forces gives predictions that are remarkably close to those obtained from more accurate calculations based on linear stability analysis.

The severe bending of the sheet in flattened "S" shapes [Fig. 7(a)] or "C" shapes [Fig. 7(b)] suggests the possibility of flow-induced self-adhesion. The "S" shape suggests the formation of folded geometries, as in Fig. 1 (top-right panel). The "C" shape may indicate the formation of rolled up configurations, potentially leading to nanoscrolls[48] (as in Fig. 1, bottom-right panel). It has been suggested that graphene can self-scroll if the radius is above a threshold of ≈10 Å.[49] From Fig. 7(b) it seems that the sheet rolls up, but then re-extends, suggesting that rolled up configurations may be achieved for $\hat{\dot{\gamma}}_L$ larger than 2000.

The two-sheets simulation results show a range of behaviors, from simple "sliding" detachment [Fig. 8(a)], to "scrolling" [Fig. 9(b)] and peeling [Fig. 10(a)]. Sliding has been reported as a dominant deformation mode in Refs. 13 and 50. Peeling has been investigated numerically in[35,51,52] and observed in experiments.[25,53] Whether sliding or peeling is a dominant mode is still an open question.[25,36,53]

In simulations of sheet pairs, the initial configuration does affect the time evolution of the shape as for the single-sheet case, but the hydrodynamic interaction between the sheets can change the tendency of a sheet to deform into an even or odd mode. For example, in Fig. 8(b) and Fig. 9(a) the sheets are initially perturbed with an odd shape, and show a "C" bending. In the single-particle case, the "C" shape is instead characteristic of an even perturbation [Fig. 7(b)].

In the experimental results of Ref. 25, the characteristic time for exfoliation was found to scale with the inverse shear rate, implying that exfoliation takes a fixed number of rotation cycles. The simulations indeed confirm that detachment requires several rotation cycles (see, e.g., Fig. 8). We can develop a simple model of pure sliding detachment by assuming that the flow profile in between the sheets is approximately a Couette flow. If the relative velocity is v_r, the viscous force resisting sliding is $\sim\mu\frac{v_r}{d}L_o$, where L_o is the overlap length. Balancing the force (per unit width) driving sliding, $\mu\dot{\gamma}L$, to the resistive viscous force gives $v_r \sim \frac{L}{L_o}d\dot{\gamma}$. With $v_r \sim L/T$, the characteristic scale for sliding is thus $T \sim \frac{L}{d}\dot{\gamma}^{-1}$. With $d/L = 0.05$, this model predict complete sliding over a timescale of $20\dot{\gamma}^{-1}$. Despite its simplicity, this model is able to predict the exfoliation time of Fig. 8(a).

Modeling peeling detachment is more complex than modeling sliding, because in peeling the motion of the peeling front is essentially controlled by the viscous dissipation at the wedge region region where the curved flap encounters the flat sheet.[53] This process has been studied in the fracture/nanomechanics literature but only for simple (typically constant) loads. In these studies, adhesion is assumed to be a requisite for peeling. Figure 9(b) illustrate that in fact a peeling-like dynamics does not require adhesion forces to be present. Sheets that are sufficiently close can be essentially glued together by the strong normal lubrication forces. This effect may be particularly important for exfoliation and dispersion in high-viscosity fluids.[54]

The results in Fig. 8(b) indicate that an important role is played, in the microscopic particle-exfoliation processes, by particle reattachment. If $\hat{\dot{\gamma}}_L$ is sufficiently large the sheets can reassemble after separating from each other. In an experiment in uniform shear, the microscopic exfoliation dynamics may thus be characterized by a cycling attachment-detachment, with no substantial pair-separation in time. For a fixed bending rigidity of the particles, increasing $\dot{\gamma}$ may thus not lead to an increase in the average particle-particle separation, as expected. This results illustrates that to obtain good dispersion of graphene in a viscous fluid (e.g., graphene sheets in a polymer nanocomposite), high shear rates do not necessarily result in good microscale dispersion, as typically assumed.

Although our work does not give a complete picture of the dynamics for the full range of parameters possible, it provides some typical shapes and recurring patterns and is therefore a starting point for those who would like to better understand the fluid dynamics of 2D nanomaterials. Despite their simplicity, 2D models are also useful for validation. Sheets that are constrained to move with their normal in the flow-gradient plane are easier to observe in experiments than sheets that complete complex 3D rotational trajectories while also deforming in three-dimensions. In future work, we will take advantage of this feature to carry out an experimental verification of the dynamics illustrated in the current paper.

A. Practical implications

The simulation results here presented may give useful insights into several applications where liquid processing of graphene or other 2D nanomaterials is used:

1. Electronics

The computed transient shapes illustrate how hydrodynamic interactions can create conditions for bending, folding and scrolling of 2D nanosheets to proceed. An ability to understand and control nanosheet topology is highly desirable as it influences material properties (e.g., electron mobility, bandgap) and has been used to tune their performance in application areas such as energy storage, electronics and optoelectronics.[55] For example, by changing the topology from planar nanosheets to nanoscrolls, the capacity performance of graphene supercapacitors increases by 50%.[56]

2. Soft robotics and wearable sensing

The application of a linear shear flow to nanosheet dispersions has practical significance for the fabrication of functional devices. Recently,

a mass production method was developed to create graphene oxide (GO) mesotubes for soft robotics and e-skins by placing nanosheet dispersions under linear shear flow conditions.[57] This process resulted in flow-induced self-organization of GO nanosheets into scrolled structures with significantly lower bandgap. These structures demonstrated sensitivity to vibration, temperature, and human artery pulse pressure. In the absence of shear flow, scrolling of sheets into tubes was not possible.

3. Material production

Scrolling of nanosheets has been observed during liquid exfoliation of graphene (Fig. 1) and other 2D materials. During continuous flow shear exfoliation of hexagonal boron nitride using a vortex fluidic device, the occurrence of nanoscrolling was found to be sensitive to flow rate, presenting an opportunity to control nanosheet topology by adjusting process parameters that alter hydrodynamic conditions.[58] The underlying mechanisms behind such selective material synthesis remain poorly understood, restricting the use of the findings to the specific production technique. Our modeling framework provides a first step to understand the origins of these shapes in shear flows more broadly.

A non-dimensional shear rate of 100 corresponds to a shear rate $\dot{\gamma} \sim 10^4\,\mathrm{s}^{-1}$ if a single-layer graphene particle of length $L \sim 0.1\ \mu$m, in a solvent of viscosity $\mu \sim 1\,\mathrm{Pa\,s}$ is considered. This indicates that with a shear rate of $10^4 - 10^5\,\mathrm{s}^{-1}$, the bending of a single sheet of graphene might be quite significant. The dynamics at these strain rates are particularly relevant to the production of defect-free 2D materials using shear exfoliation. Experimental evidence indicates that shear rates above $\sim 10^4\,\mathrm{s}^{-1}$ are necessary for effective exfoliation of graphene and other 2D materials such as MoS_2 and WS_2.[59] The fact that the threshold for buckling and the threshold for exfoliation have similar magnitudes may suggest that severe bending is a prerequisite for high-yield exfoliation of larger sheets (which could bend at accessible shear rates, see discussion in Ref. 36).

4. Material quality assurance

The sensitive structure-property relationship of 2D materials highlights the importance of performing minimally invasive material characterization for quality assurance of production batches. The preparation of samples for microscopy [e.g., TEM, Atomic Force Microscope (AFM) and SEM] and spectroscopy (e.g., Raman, UV-Vis-nIR) techniques naturally require handling of nanomaterial dispersions. Pipetting is the main technique used to extract samples from production processes and to transfer samples to characterization suites for analysis. In biological sciences, excessive shear stress caused by pipet triturations can adversely affect biological material.[60] For nanosheet dispersions, an unforced, standard pipetting approach would typically result in an elasto-viscous number ~ 0.1. This implies the nanosheet structure is unlikely to be altered by mild pipetting actions. However, vigorous pipetting or triturations to re-disperse partially agglomerated nanosheets could promote morphology changes. This is quantifiable using the findings in this study, enabling the development of sampling protocols for minimally invasive material characterization in laboratories and industry alike.

5. Functional composites and inks

The possibility of particle bending is quite realistic in these high-fluid-stress applications, either because of the large fluid viscosity (e.g., in polymer nanocomposites), or because of the large shear rates (e.g., in ink-jet printing or high-speed coating). In nanocomposites, the threshold shear rate for buckling should ideally not be reached, as the best performance is obtained when the graphene nanofillers are extended and not crumpled. In printing, avoiding clogging is paramount, so a fundamental understanding of particle-particle hydrodynamic interactions is crucial. The simulations in this paper not only give a quantification of the non-dimensional shear rate for which highly curved morphology are obtained, potentially leading to self-adhesion, but also illustrate the effect of a small inter-particle separation. It is expected that changes in shape at a critical buckling threshold will have signatures in the rheological response of composite and inks with suspended sheet like particles, as already demonstrated in dilute suspensions of fibers or stiff polymers.[61] Our results indicate that deformation modes of two particles in close proximity may be very different from those of isolated particles.

6. Other considerations on liquid-phase exfoliation

Regarding liquid-phase exfoliation, one might wonder whether the unbounded, steady, simple shear flow configuration considered in this paper is a good model for the flow in an actual exfoliation process, and whether computed transient shapes in our simulations could give insights into the final shape of the sheets in actual experiments. Regarding the first question, admittedly a simple shear flow is a crude representation of a realistic flow, such as the flow in a high-speed homogenizer. However, exfoliation experiments conducted with a Couette device at a controlled mean shear rate, and with a homogenizer producing the same average shear rate as in the Couette device, have produced very similar exfoliation outcomes.[13] This suggests that the mean shear is the key controlling variable, thus justifying the study of a steady, laminar flow. The assumption of an unbounded system is not very restrictive given the extremely small length of 2D nanosheets ($\sim 1\ \mu$m) compared to even the smallest gap sizes present in mixers/homogenizer (~ 1 mm). The second question is more delicate. In real systems, such as liquid exfoliation and processing of functional inks, the stability of the nanosheet shapes depends on non-hydrodynamic factors including adhesion, electrostatic repulsion, capillary forces following drying, and steric exclusion effects.[62,63] While these additional factors are necessary to maintain stable nanosheet morphologies, the emergence of different shapes arises with external forcing, e.g., mixing and shear.[57,58,62] If suitable care is taken in the material preparation and characterization steps (see "Material quality assurance"), the formation of these shapes can be attributed to the mixing or other high shear processes. Indeed the dominance of shear exfoliation on the final shapes has been demonstrated indirectly by previous work on hexagonal boron nitride nanosheets.[58] Adjusting processing parameters changed the product from nanosheets to nanoscrolls. These differences in final shape can be attributed to the shear exfoliation conditions as the authors used identical post-production and material characterization steps on all samples produced. The permanence of flow-induced shapes is also critically important in the processing of graphene nanocomposites, in which the fast solidification of the polymer melt following, e.g., extrusion, "freezes" the morphology induced by shear forces almost instantaneously. In these applications, the viscosity of the fluid is high (the shear viscosity in polymer mixing typically ranges from 0.01 to 10 Pa s,[64] and higher viscosity values of

thousands of Pa s have been measured in specialized applications) and thus lubrication interactions between particles will be important. In view of this application area, the study of close range hydrodynamic interactions similar to those investigated in the current study can help understanding the conditions under which particle-particle deagglomeration can be obtained.

V. CONCLUSIONS

We have carried out simulations of isolated or interacting elastic sheets in simple steady shear flow to get insights into the type of morphology one might obtain when subjecting graphene or other 2D materials to shearing flows. Our work provides insights into the flow micro-physics, typical flow-induced morphologies, and recurring dynamic patterns, and is therefore a starting point for those who would like to better understand the fluid dynamics of graphene and other 2D nanomaterials. Rather than limiting ourselves to describe the physics, we attempt to translate the observations into practical recommendations, which are given in Sec. IV.

In the simulations we have neglected non-hydrodynamic inter-particle interactions, such as van der Waals forces or electrostatic forces. In the context of 2D materials, electrostatic forces are predominantly repulsive and of varying range, while van der Waals forces are attractive and short-ranged. Sufficiently strong electrostatic forces would lead to an increase in inter-particle separation (in the two-particle case) and would limit the occurrence of high curvatures in each sheet's shape (due to self-repulsion). Attractive van der Waals would act in the opposite direction. Attractive forces are particularly important at small surface-to-surface separations, thus competing with lubrication forces and potentially making the transient, highly curved C-shaped configuration, such as those in Fig. 7, permanent via self-adhesion; an outcome, this latter, which could change effectively the shape of the particles and therefore the rheological response of a suspension.[61] In a previous study[65] we have implemented a simple linearized model of van der Waals interactions in our code. In that case, we did not use the line integral approach, but simplified the fluid-structure interaction using a local drag model. A similar adhesive force can be easily implemented in the method described in the current paper.

Future work should consider more complex particle geometries and full three-dimensional simulations. The simulation model we consider is essentially two dimensional, as the rotation of the particles is constrained to be in the flow-gradient plane, so future work should consider interacting three-dimensional sheets moving in three dimensions. The consideration of 2D simulations however has a key advantage. Despite their simplicity, 2D models are useful for experimental validation. Sheets that are constrained to move with their normal in the flow-gradient plane are easier to observe in experiments than sheets that complete complex 3D rotational trajectories while also deforming in three-dimensions. In future work, we will take advantage of this feature to carry out an experimental verification of the dynamics illustrated in the current paper. Another aspect to consider is the effect of hydrodynamic slip. We have assumed no-slip boundary conditions, which is a good model for heavily functionalized or oxidized graphene,[27] but graphene has a rather large slip length, and this can affect the dynamics of pristine graphene sheets.[2,16,26,36] How slip affects the dynamics of interacting, deformable sheets is an open question.

ACKNOWLEDGMENTS

This work was funded by the European Research Council, under the European Union's Horizon 2020 Research and Innovation programme (Project flexnanoflow, Grant Agreement No. 715475).

AUTHOR DECLARATIONS

Conflict of Interest

The authors have no conflicts to disclose.

DATA AVAILABILITY

The data that support the findings of this study are available from the corresponding authors upon reasonable request.

REFERENCES

[1]K. El Haddad, C. Aumnate, C. Saengow, M. Kanso, S. Coombs, and A. Giacomin, "Complex viscosity of graphene suspensions," Phys. Fluids **33**, 093109 (2021).
[2]C. Kamal, S. Gravelle, and L. Botto, "Alignment of a flexible platelike particle in shear flow: Effect of surface slip and edges," Phys. Rev. Fluids **6**, 084102 (2021).
[3]K. S. Silmore, M. Strano, and J. W. Swan, "Thermally fluctuating, semiflexible sheets in simple shear flow," Soft Matter **18**, 768 (2022).
[4]Y. Yu and M. D. Graham, "Wrinkling and multiplicity in the dynamics of deformable sheets in uniaxial extensional flow," Phys. Rev. Fluids **7**(2) 023601 (2022).
[5]B. Derby and N. Reis, "Inkjet printing of highly loaded particulate suspensions," MRS Bull. **28**, 815–818 (2003).
[6]Q. Mei and Z. Zhang, "Photoluminescent graphene oxide ink to print sensors onto microporous membranes for versatile visualization bioassays," Angew. Chem., Int. Ed. **51**, 5602 (2012).
[7]C. Grotta, "3d printing of transition metal dichalcogenides," Ph.D. thesis (Imperial College London, 2018); available at https://spiral.imperial.ac.uk/handle/10044/1/67288.
[8]J. C. Spear, B. W. Ewers, and J. D. Batteas, "2D-nanomaterials for controlling friction and wear at interfaces," Nano Today **10**, 301–314 (2015).
[9]M. Zhang, Y. Ma, Y. Zhu, J. Che, and Y. Xiao, "Two-dimensional transparent hydrophobic coating based on liquid-phase exfoliated graphene fluoride," Carbon **63**, 149–156 (2013).
[10]X. Fu and S. Qutubuddin, "Polymer–clay nanocomposites: Exfoliation of organophilic montmorillonite nanolayers in polystyrene," Polymers **42**, 807–813 (2001).
[11]S. Barwich, J. N. Coleman, and M. E. Möbius, "Yielding and flow of highly concentrated, few-layer graphene suspensions," Soft Matter **11**, 3159–3164 (2015).
[12]N. K. Borse and M. R. Kamal, "Estimation of stresses required for exfoliation of clay particles in polymer nanocomposites," Polym. Eng. Sci. **49**, 641–650 (2009).
[13]K. R. Paton, E. Varrla, C. Backes, R. J. Smith, U. Khan, A. O'Neill, C. Boland, M. Lotya, O. M. Istrate, P. King *et al.*, "Scalable production of large quantities of defect-free few-layer graphene by shear exfoliation in liquids," Nat. Mater. **13**, 624–630 (2014).
[14]K. S. Silmore, M. S. Strano, and J. W. Swan, "Buckling, crumpling, and tumbling of semiflexible sheets in simple shear flow," Soft Matter **17**, 4707–4718 (2021).
[15]Y. Yu and M. D. Graham, "Coil–stretch-like transition of elastic sheets in extensional flows," Soft Matter **17**(3), 543–553 (2021).
[16]S. Gravelle, C. Kamal, and L. Botto, "Violations of Jeffrey's theory in the dynamics of nanographene in shear flow," Phys. Rev. Fluids **6**, 034303 (2021).
[17]Y. Xu and M. J. Green, "Brownian dynamics simulations of nanosheet solutions under shear," J. Chem. Phys **141**, 024905 (2014).
[18]S. B. Babu and H. Stark, "Dynamics of semi-flexible tethered sheets," Eur. Phys. J. E **34**, 136 (2011).
[19]O. Du Roure, A. Lindner, E. N. Nazockdast, and M. J. Shelley, "Dynamics of flexible fibers in viscous flows and fluids," Annu. Rev. Fluid Mech. **51**, 539–572 (2019).

[20]L. J. Fauci and C. S. Peskin, "A computational model of aquatic animal locomotion," J. Comput. Phys. **77**, 85–108 (1988).
[21]J. Simons, L. Fauci, and R. Cortez, "A fully three-dimensional model of the interaction of driven elastic filaments in a Stokes flow with applications to sperm motility," J. Biomech. **48**, 1639–1651 (2015).
[22]A.-K. Tornberg and M. J. Shelley, "Simulating the dynamics and interactions of flexible fibers in stokes flows," J. Comput. Phys. **196**, 8–40 (2004).
[23]L. H. Li, Y. Chen, G. Behan, H. Zhang, M. Petravic, and A. M. Glushenkov, "Large-scale mechanical peeling of boron nitride nanosheets by low-energy ball milling," J. Mater. Chem. **21**, 11862–11866 (2011).
[24]V. Nicolosi, M. Chhowalla, M. G. Kanatzidis, M. S. Strano, and J. N. Coleman, "Liquid exfoliation of layered materials," Science **340**, 1226419 (2013).
[25]J. Stafford, N. Uzo, U. Farooq, S. Favero, S. Wang, H.-H. Chen, A. L'Hermitte, C. Petit, and O. K. Matar, "Real-time monitoring and hydrodynamic scaling of shear exfoliated graphene," 2D Mater. **8**, 025029 (2021).
[26]C. Kamal, S. Gravelle, and L. Botto, "Effect of hydrodynamic slip on the rotational dynamics of a thin Brownian platelet in shear flow," J. Fluid Mech. **919**, A1 (2021).
[27]C. Kamal, S. Gravelle, and L. Botto, "Hydrodynamic slip can align thin nanoplatelets in shear flow," Nat. Commun. **11**, 1–10 (2020).
[28]D. J. Smith, "A boundary element regularized Stokeslet method applied to cilia-and flagella-driven flow," Proc. R. Soc., A **465**, 3605–3626 (2009).
[29]S. D. Olson and L. J. Fauci, "Hydrodynamic interactions of sheets vs filaments: Synchronization, attraction, and alignment," Phys. Fluids **27**, 121901 (2015).
[30]T. D. Montenegro-Johnson, L. Koens, and E. Lauga, "Microscale flow dynamics of ribbons and sheets," Soft Matter **13**, 546–553 (2017).
[31]G. Batchelor, "Slender-body theory for particles of arbitrary cross-section in stokes flow," J. Fluid Mech. **44**, 419–440 (1970).
[32]C. Pozrikidis, *Boundary Integral and Singularity Methods for Linearized Viscous Flow* (Cambridge University Press, 1992).
[33]R. Cortez, "The method of regularized stokeslets," SIAM J. Sci. Comput. **23**, 1204–1225 (2001).
[34]V. Singh, D. L. Koch, G. Subramanian, and A. D. Stroock, "Rotational motion of a thin axisymmetric disk in a low Reynolds number linear flow," Phys. Fluids **26**, 033303 (2014).
[35]G. Salussolia, E. Barbieri, N. M. Pugno, and L. Botto, "Micromechanics of liquid-phase exfoliation of a layered 2D material: A hydrodynamic peeling model," J. Mech. Phys. Solids **134**, 103764 (2020).
[36]S. Gravelle, C. Kamal, and L. Botto, "Liquid exfoliation of multilayer graphene in sheared solvents: A molecular dynamics investigation," J. Chem. Phys. **152**, 104701 (2020).
[37]J. M. Stockie and S. I. Green, "Simulating the motion of flexible pulp fibres using the immersed boundary method," J. Comput. Phys. **147**, 147–165 (1998).
[38]E. Guazzelli and J. F. Morris, *A Physical Introduction to Suspension Dynamics* (Cambridge University Press, 2011), Vol. 45.
[39]S. Kim and S. J. Karrila, *Microhydrodynamics: Principles and Selected Applications* (Courier Corporation, 2013).
[40]C. Lee, X. Wei, J. W. Kysar, and J. Hone, "Measurement of the elastic properties and intrinsic strength of monolayer graphene," Science **321**, 385–388 (2008).
[41]L. E. Becker and M. J. Shelley, "Instability of elastic filaments in shear flow yields first-normal-stress differences," Phys. Rev. Lett. **87**, 198301 (2001).
[42]O. Forgacs and S. Mason, "Particle motions in sheared suspensions: X. orbits of flexible threadlike particles," J. Colloid Sci. **14**, 473–491 (1959).
[43]N. Quennouz, M. Shelley, O. du Roure, and A. Lindner, "Transport and buckling dynamics of an elastic fibre in a viscous cellular flow," J. Fluid Mech. **769**, 387–402 (2015).
[44]P. Lingard and R. Whitmore, "The deformation of disc-shaped particles by a shearing fluid with application to the red blood cell," J. Colloid Interface Sci. **49**, 119–127 (1974).
[45]K. White, S. Hawkins, M. Miyamoto, A. Takahara, and H.-J. Sue, "Effects of aspect ratio and concentration on rheology of epoxy suspensions containing model plate-like nanoparticles," Phys. Fluids **27**, 123306 (2015).
[46]C. Dhong and J. Fréchette, "Peeling flexible beams in viscous fluids: Rigidity and extensional compliance," J. Appl. Phys. **121**, 044906 (2017).
[47]B. Chakrabarti, Y. Liu, J. LaGrone, R. Cortez, L. Fauci, O. du Roure, D. Saintillan, and A. Lindner, "Flexible filaments buckle into helicoidal shapes in strong compressional flows," Nat. Phys. **16**, 689–694 (2020).
[48]X. Li, X. Hao, M. Zhao, Y. Wu, J. Yang, Y. Tian, and G. Qian, "Exfoliation of hexagonal boron nitride by molten hydroxides," Adv. Mater. **25**, 2200–2204 (2013).
[49]D. Xia, Q. Xue, J. Xie, H. Chen, C. Lv, F. Besenbacher, and M. Dong, "Fabrication of carbon nanoscrolls from monolayer graphene," Small **6**, 2010–2019 (2010).
[50]X. Chen, J. F. Dobson, and C. L. Raston, "Vortex fluidic exfoliation of graphite and boron nitride," Chem. Commun. **48**, 3703–3705 (2012).
[51]V. Sresht, A. A. Padua, and D. Blankschtein, "Liquid-phase exfoliation of phosphorene: Design rules from molecular dynamics simulations," ACS Nano **9**, 8255–8268 (2015).
[52]R. C. Sinclair, J. L. Suter, and P. V. Coveney, "Graphene–graphene interactions: Friction, superlubricity, and exfoliation," Adv. Mater. **30**, 1705791 (2018).
[53]L. Botto, "Towards nanomechanical models of liquid-phase exfoliation of layered 2D nanomaterials: Analysis of a π-peel model," Front. Mater. **6**, 302 (2019).
[54]G. Santagiuliana, O. T. Picot, M. Crespo, H. Porwal, H. Zhang, Y. Li, L. Rubini, S. Colonna, A. Fina, E. Barbieri *et al.*, "Breaking the nanoparticle loading–dispersion dichotomy in polymer nanocomposites with the art of croissant-making," ACS Nano **12**, 9040–9050 (2018).
[55]X. Li, L. Tao, Z. Chen, H. Fang, X. Li, X. Wang, J.-B. Xu, and H. Zhu, "Graphene and related two-dimensional materials: Structure-property relationships for electronics and optoelectronics," Appl. Phys. Rev. **4**, 021306 (2017).
[56]F. Zeng, Y. Kuang, G. Liu, R. Liu, Z. Huang, C. Fu, and H. Zhou, "Supercapacitors based on high-quality graphene scrolls," Nanoscale **4**, 3997–4001 (2012).
[57]G. M. Choi, M. Park, Y. H. Shim, S. Y. Kim, and H. S. Lee, "Mass production of 2D manifolds of graphene oxide by shear flow," Adv. Funct. Mater. **32**, 2107694 (2022).
[58]A. H. M. Al-Antaki, X. Luo, T. M. Alharbi, D. P. Harvey, S. Pye, J. Zou, W. Lawrance, and C. L. Raston, "Inverted vortex fluidic exfoliation and scrolling of hexagonal-boron nitride," RSC Adv. **9**, 22074–22079 (2019).
[59]S. Biccai, S. Barwich, D. Boland, A. Harvey, D. Hanlon, N. McEvoy, and J. N. Coleman, "Exfoliation of 2D materials by high shear mixing," 2D Mater. **6**, 015008 (2018).
[60]Y. Xie, F. Wang, E. Puscheck, and D. Rappolee, "Pipetting causes shear stress and elevation of phosphorylated stress-activated protein kinase/Jun kinase in preimplantation embryos," Mol. Reprod. Dev. **74**, 1287–1294 (2007).
[61]B. Chakrabarti, Y. Liu, O. Du Roure, A. Lindner, and D. Saintillan, "Signatures of elastoviscous buckling in the dilute rheology of stiff polymers," J. Fluid Mech. **919**, A12 (2021).
[62]B. Tang, E. Gao, Z. Xiong, B. Dang, Z. Xu, and X. Wang, "Transition of graphene oxide from nanomembrane to nanoscroll mediated by organic solvent in dispersion," Chem. Mater. **30**, 5951–5960 (2018).
[63]M. Trushin and A. C. Neto, "Stability of a rolled-up conformation state for two-dimensional materials in aqueous solutions," Phys. Rev. Lett. **127**, 156101 (2021).
[64]Y. Y. Huang and E. M. Terentjev, "Dispersion of carbon nanotubes: Mixing, sonication, stabilization, and composite properties," Polymers **4**, 275–295 (2012).
[65]G. Salussolia, "A numerical study of the flow dynamics of graphene sheets based on continuum simulations," Ph.D. thesis (Queen Mary University of London, 2019).